The Astrophysical Journal, 856:55 (11pp), 2018 March 20 https://doi.org/10.3847/1538-4357/aaae64

Simultaneous 13 cm/3 cm Single-pulse Observations of PSR B0329+54

Zhen Yan (闫振)[1,8], Zhi-Qiang Shen (沈志强)[1,8], R. N. Manchester[2], C.-Y. Ng[3], P. Weltevrede[4], Hong-Guang Wang (王洪光)[5], Xin-Ji Wu (吴鑫基)[6], Jian-Ping Yuan (袁建平)[7,8], Ya-Jun Wu (吴亚军)[1,8], Rong-Bing Zhao (赵融冰)[1,8], Qing-Hui Liu (刘庆会)[1,8], Ru-Shuang Zhao (赵汝双)[1,9], and Jie Liu (刘杰)[1,9]

[1] Shanghai Astronomical Observatory, Chinese Academy of Sciences, Shanghai 200030, People's Republic of China; yanzhen@shao.ac.cn
[2] CSIRO Astronomy and Space Science, P.O. Box 76, Epping NSW 1710, Australia
[3] Department of Physics, The University of Hong Kong, Pokfulam Road, Hong Kong, People's Republic of China
[4] Jodrell Bank Centre for Astrophysics, School of Physics and Astronomy, University of Manchester, Manchester M13 9PL, UK
[5] School of Physics and Electronic Engineering, Guangzhou University, 510006 Guangzhou, People's Republic of China
[6] Department of Astronomy, Peking University, Beijing 100871, People's Republic of China
[7] Xinjiang Astronomical Observatory, Chinese Academy of Sciences, Urumqi 830011, People's Republic of China
[8] Key Laboratory of Radio Astronomy, Chinese Academy of Sciences, People's Republic of China
[9] University of Chinese Academy of Sciences, Beijing 100049, People's Republic of China
Received 2017 September 14; revised 2018 February 7; accepted 2018 February 7; published 2018 March 23

Abstract

We have investigated the mode changing properties of PSR B0329+54 using 31 epochs of simultaneous 13 cm/3 cm single-pulse observations obtained with the Shanghai Tian Ma 65 m telescope. The pulsar was found in the abnormal emission mode 17 times, accounting for ~13% of the 41.6 hr total observation time. Single-pulse analyses indicate that mode changes took place simultaneously at 13 cm/3 cm within a few rotational periods. We detected occasional bright and narrow pulses whose peak flux densities were 10 times higher than that of the integrated profile in both bands. At 3 cm, about 0.66% and 0.27% of single pulses were bright in the normal mode and abnormal mode, respectively, but at 13 cm the occurrence rate was only about 0.007%. We divided the pulsar radiation window into three components (C1, C2, and C3) corresponding to the main peaks of the integrated profile. The bright pulses preferentially occurred at pulse phases corresponding to the peaks of C2 and C3. Fluctuation spectra showed that C2 had excess red noise in the normal mode, but broad quasi-periodic features with central frequencies around 0.12 cycles/period in the abnormal mode. At 3 cm, C3 had a stronger quasi-periodic modulation centered around 0.06 cycles/period in the abnormal mode. Although there were some asymmetries in the two-dimensional fluctuation spectra, we found no clear evidence for systematic subpulse drifting. Consistent with previous low-frequency observations, we found a very low nulling probability for B0329+54, with upper limits of 0.13% and 1.68% at 13 cm/3 cm, respectively.

Key words: pulsars: individual (B0329+54)

1. Introduction

Pulsars are fast-rotating, highly magnetized neutron stars that produce lighthouse-like beams of radio emission from their magnetic poles. The pulsed radiation can only be observed when the emission beam is pointing toward the Earth, forming a pulse train with an extremely stable period. In practice, observers can only detect individual pulses from comparatively strong pulsars, as pulsars are intrinsically weak radio sources.

In order to improve the signal-to-noise ratio (S/N) of pulsar observations, the integrated profile is usually used. The integrated profile is obtained by summing up a number of individual pulses synchronously with the rotational period. For most pulsars, the shape of individual pulses varies dramatically from pulse to pulse, while the integrated profile is very stable at any particular observing frequency (Helfand et al. 1975). However, integrated profiles for some pulsars show sporadic changes between two (sometimes more than two) quasi-stable states; this is called mode changing or switching. Ever since the first detection of mode changes in PSR B1237+25 (Backer 1970), this phenomenon has been seen in a few dozens of pulsars in subsequent years (Lyne 1971; Ferguson et al. 1981; Morris et al. 1981; Wright & Fowler 1981), with a continued increase in recent times (e.g., Wang et al. 2007; Burke-Spolaor et al. 2012). Most of these pulsars have a complex integrated profile with multiple components.

Some of the pulsars that show mode changes also exhibit drifting subpulses (van Leeuwen et al. 2002; Janssen & van Leeuwen 2004; Redman et al. 2005). But the connection between these two phenomena is not well understood yet. It appears that young pulsars have the most disordered subpulses and that drifting subpulses are more often seen in older pulsars (Rankin 1986). Simultaneous multi-frequency single-pulse observations are the most direct way to study whether the mode changing and subpulse drifting are wide-band phenomena and to study the intrinsic relationships between mode changes and subpulse drifts. Most previous observations indicated that these two phenomena took place synchronously over a wide band. However, there are exceptions, e.g., PSR B0031−07, where in simultaneous 328 MHz and 4.85 GHz observations (Smits et al. 2005), only mode A occurred at the same time at both frequencies, while modes B and C only occurred at 328 MHz.

PSR B0329+54 is a pulsar showing a complex integrated profile that can be fitted with five Gaussian components (Kramer 1994). Long-term low-frequency observations indicated that this pulsar shows relatively frequent mode changes,

Table 1
Measured and Derived Parameters of PSR B0329+54

Parameters	Values	Unit	References
P	0.714520	s	Hobbs et al. (2004)
$\dot{P}$	2.05×10^{-15}	⋯	Hobbs et al. (2004)
DM	26.7641	cm^{-3} pc	Hassall et al. (2012)
S_{1400}	203	mJy	Lorimer et al. (1995)
α	−1.6	⋯	Lorimer et al. (1995)
D	1.0	kpc	Yao et al. (2017)
τ	5.53×10^{6}	year	⋯
B_s	1.22×10^{12}	G	⋯
B_{LC}	31.5	G	⋯
$\dot{E}$	2.22×10^{32}	erg s^{-1}	

Note. The listed parameters are the barycentric period (P), time derivative of the barycentric period ($\dot{P}$), dispersion measure (DM), mean flux density at 1400 MHz (S_{1400}), spectral index (α), DM-derived distance based on the YMW16 model (D), spin-down age (τ), surface magnetic flux density (B_s), magnetic field at light cylinder (B_{LC}), and spin-down luminosity ($\dot{E}$).

with the pulsar in an "abnormal" mode ∼15% of the time (Bartel et al. 1982; Chen et al. 2011).

In Table 1, we list the basic measured and derived parameters of PSR B0329+54.[10] At a frequency ν of 1.4 GHz, the mean flux density of PSR B0329+54 is about 230 mJy, with a spectral index α ($S_\nu \propto \nu^\alpha$) of about −1.6 (Lorimer et al. 1995). Because of its strong flux density and somewhat flat spectrum, the mode changes of this pulsar have also been detected at high frequencies, such as 10.5 GHz (Xilouris et al. 1995), 14.8 GHz (Bartel & Sieber 1978), 32 GHz (Kramer et al. 1996), and 43 GHz (Kramer et al. 1997). Dual-band single-pulse observations of PSR B0329+54 have been carried out, for example, at 327 and 2695 MHz (Bartel & Sieber 1978), and 1.4 and 9.0 GHz (Bartel et al. 1982). Except for the 327 MHz/2695 MHz observations that were carried out with a dual-band receiver, the others made use of simultaneous observations on different telescopes. In all of these observations, the mode changes occurred synchronously at the two different frequencies.

In this paper, we report simultaneous single-pulse observations of PSR B0329+54 in the 13 cm and 3 cm bands (with corresponding center frequencies of 2.3 GHz and 8.6 GHz) with the Shanghai Tian Ma Radio Telescope (TMRT) in order to study the mode changes and related phenomena with a comparatively wide frequency coverage. The observations and data reduction methods are described in Section 2. Detail about the analyses of mode changes, bright narrow pulses, subpulse drifting, and pulse-nulling are presented in Sections 3, 4, 5, and 6, respectively. A discussion and conclusions are given in Section 7.

2. Observations and Data Reduction

Observations of PSR B0329+54 were carried out with the TMRT, which is a fully steerable 65 m diameter Cassegrain antenna with an active reflector surface. Seven sets of receivers are installed, with the frequency coverage ranging from 1.25 to 50.0 GHz. Taking the power-law spectrum radiation with the spectral index of −1.6 into consideration, the 13 cm/3 cm receiver was selected to do simultaneous dual-frequency

[10] Data from the ATNF Pulsar Catalog, http://www.atnf.csiro.au/research/pulsar/psrcat (Manchester et al. 2005).

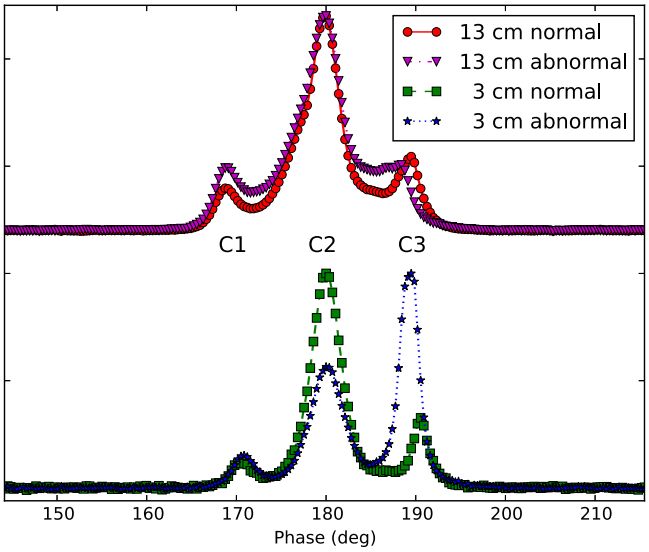

Figure 1. Typical normal and abnormal mode integrated profiles of PSR B0329+54 obtained at 13 cm/3 cm, with the principal pulse components identified.

observations of PSR B0329+54. This 13 cm/3 cm receiver is a cryogenically cooled, dual-polarization and dual-band receiver with frequency coverages of 2.2–2.4 GHz and 8.2–9.0 GHz in the 13 cm and 3 cm bands, respectively. Normally, the system equivalent flux density (SEFD) of the TMRT is about 46 Jy and 48 Jy at 13 cm and 3 cm, respectively.

The digital backend system (DIBAS), an FPGA-based spectrometer based upon the design of VEGAS (Anish Roshi et al. 2012) with pulsar modes that provide much the same capabilities as GUPPI (DuPlain et al. 2008), was used for the data sampling and recording. DIBAS has three pairs of digitizers (one for each polarization pair), making it possible to sample and digitize data from different bands (Yan et al. 2015). Our observations used pulsar search mode and the signals from the 13 cm and 3 cm were sampled by the first two digitizer pairs. The received bandwidths, 200 MHz and 800 MHz for 13 cm and 3 cm, respectively, were each divided into 512 channels to allow mitigation of radio-frequency interference (RFI) and offline dedispersion. In order to reduce the data rate, we chose to record total intensity (i.e., Stokes I) only by summing the two polarization channels after digitization. The data from each receiver were written out separately as an 8-bit PSRFITS (Hotan et al. 2004) file. Observing parameters are listed in the first four columns of Table 2. They are, respectively, the epoch number (N), observation start time as a Modified Julian Date (MJD), observation length (T_o), and sampling interval (t_{samp}). At the time of our observations, the diodes that inject pulsed signals into the front end of each receiver had not been installed. Before starting each observation, a careful adjustment was made to ensure that the power levels of the left and right polarization channels were at the level of −20.0 dBm with an accuracy better than 0.5 dBm.

At 13 cm, telecommunication RFI seriously affected the observational data, with only about 100 MHz of reasonably clean bandwidth left for each epoch of observation. At 3 cm, RFI was seldom a problem and the entire 800 MHz bandwidth was kept for further analyses. After RFI rejection, channels were summed using incoherent dedispersion to give a single

Table 2
Observation Parameters and Mode Change Statistics for PSR B0329+54

N	MJD	T_o (s)	t_{samp} (μ s)	M_A	T_A (s)	$S_{A/N,13\ cm}$	$S_{A/N,3\ cm}$
1	56755.33	1636	65.54	Y	590 ± 5	0.08 ± 0.01	0.21 ± 0.14
2	56759.10	4648	65.54	Y	875 ± 3	0.47 ± 0.01	0.16 ± 0.11
3	56759.17	3729	65.54	N	0	...	...
4	56759.23	2857	65.54	N	0	...	...
5	56759.42	2641	65.54	Y	2641 ± 1	...	...
6	56761.08	1685	65.54	Y	1685 ± 1		
7	56782.12	1866	32.77	N	0	...	...
8	56782.19	2556	32.77	N	0	...	...
9	56782.28	3399	32.77	N	0	...	...
10	56784.07	7187	65.54	N	0	...	...
11	56784.15	7187	131.07	N	0	...	...
12	56784.24	7187	131.07	Y	782 ± 4	−0.55 ± 0.01	0.29 ± 0.08
13	56784.32	4233	131.07	Y	875 ± 4	0.22 ± 0.02	0.05 ± 0.06
14	56785.08	7188	131.07	N	0	...	...
15	56785.12	7188	131.07	Y	222 ± 5	−0.43 ± 0.02	−0.12 ± 0.07
16	56785.20	7188	131.07	Y	1477 ± 6/235 ± 3	0.37 ± 0.01	0.02 ± 0.03
17	56785.28	7188	131.07	Y	4579 ± 3	−0.12 ± 0.01	0.10 ± 0.02
18	56786.04	7188	131.07	N	0	...	...
19	56786.12	1626	131.07	N	0	...	...
20	56786.31	5594	131.07	Y	154 ± 2/289 ± 3	0.01 ± 0.03	0.21 ± 0.04
21	56836.04	7188	131.07	N	0	...	...
22	56836.16	6733	131.07	Y	245 ± 6	0.30 ± 0.02	0.11 ± 0.14
23	56850.11	3580	131.07	N	0	...	...
24	56863.06	2437	131.07	N	0	...	...
25	56863.10	7188	131.07	N	0	...	...
26	56863.96	4061	131.07	Y	2153 ± 7	0.51 ± 0.02	0.30 ± 0.04
27	56950.62	5395	65.54	Y	900 ± 6	0.23 ± 0.01	0.23 ± 0.03
28	56950.68	5395	65.54	N	0	...	...
29	56950.74	5395	65.54	N	0	...	...
30	56950.81	6189	65.54	Y	1486 ± 4	−0.20 ± 0.01	0.09 ± 0.02
31	56951.68	2396	65.54	Y	90 ± 5	−0.11 ± 0.05	0.21 ± 0.14

Note. The epoch number (N), observation start time as a modified julian date (MJD), observation length (T_o), and sampling interval (t_{samp}) are listed in the first four columns of this table, respectively. The marks "Y" and "N" given in the fifth column (M_A) indicate detection or non-detection of the abnormal mode in the corresponding observation. The length of the abnormal mode (T_A) is presented in the sixth column. In cases where there were two or more blocks of abnormal mode in that epoch of observation, the duration of each abnormal mode block is given. The final two columns give the parameters $S_{A/N} \equiv (S_A - S_N)/(S_A + S_N)$ for the 13 cm and 3 cm bands, respectively, where S_A and S_N are mean pulsed flux densities for the abnormal and normal modes.

data stream for each band. These were converted to single-pulse time series by folding the data at the predicted topocentric period using polynomial coefficients generated with TEMPO2 (Hobbs et al. 2006). The single-pulse series were written out with 1024 phase bins per period in the PSRFITS format. The PSRCHIVE programs (Hotan et al. 2004) were used for further data editing and processing.

3. Mode Changes in PSR B0329+54

3.1. Mode Change Detection

Pulsar mode changes are sporadic and abrupt switches of the integrated profile between at least two quasi-stable states. In Figure 1, we present typical normal and abnormal integrated profiles of PSR B0329+54 obtained with our 13 cm/3 cm observations. At both 13 cm and 3 cm the mean pulse profiles have three main peaks denoted by C1, C2, and C3. The most significant feature of the mode change in PSR B0329+54 is the change in the peak strength and position of C3, especially at 3 cm. At 13 cm, C3 moves to an earlier phase, decreases in strength, and merges with the bridge between C2 and C3. At 3 cm, similar to 13 cm, C3 moves to an earlier phase (by about 1°), but unlike at 13 cm, increases considerably in strength, and becomes stronger than C2.

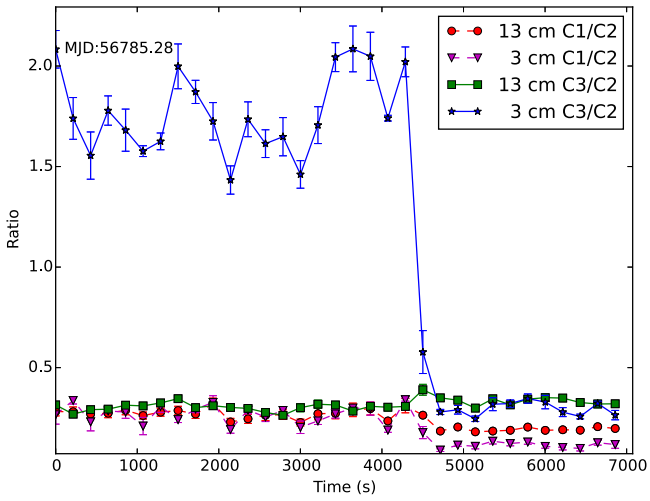

Figure 2. Time sequence of peak intensity ratios C1/C2 and C3/C2 at 13 cm and 3 cm for PSR B0329+54. This sequence started at MJD 56785.28.

The peak intensity ratio of the leading (C1) and the trailing (C3) components relative to the central peak (C2), labeled as C1/C2 and C3/C2, were used as indicators for potential mode

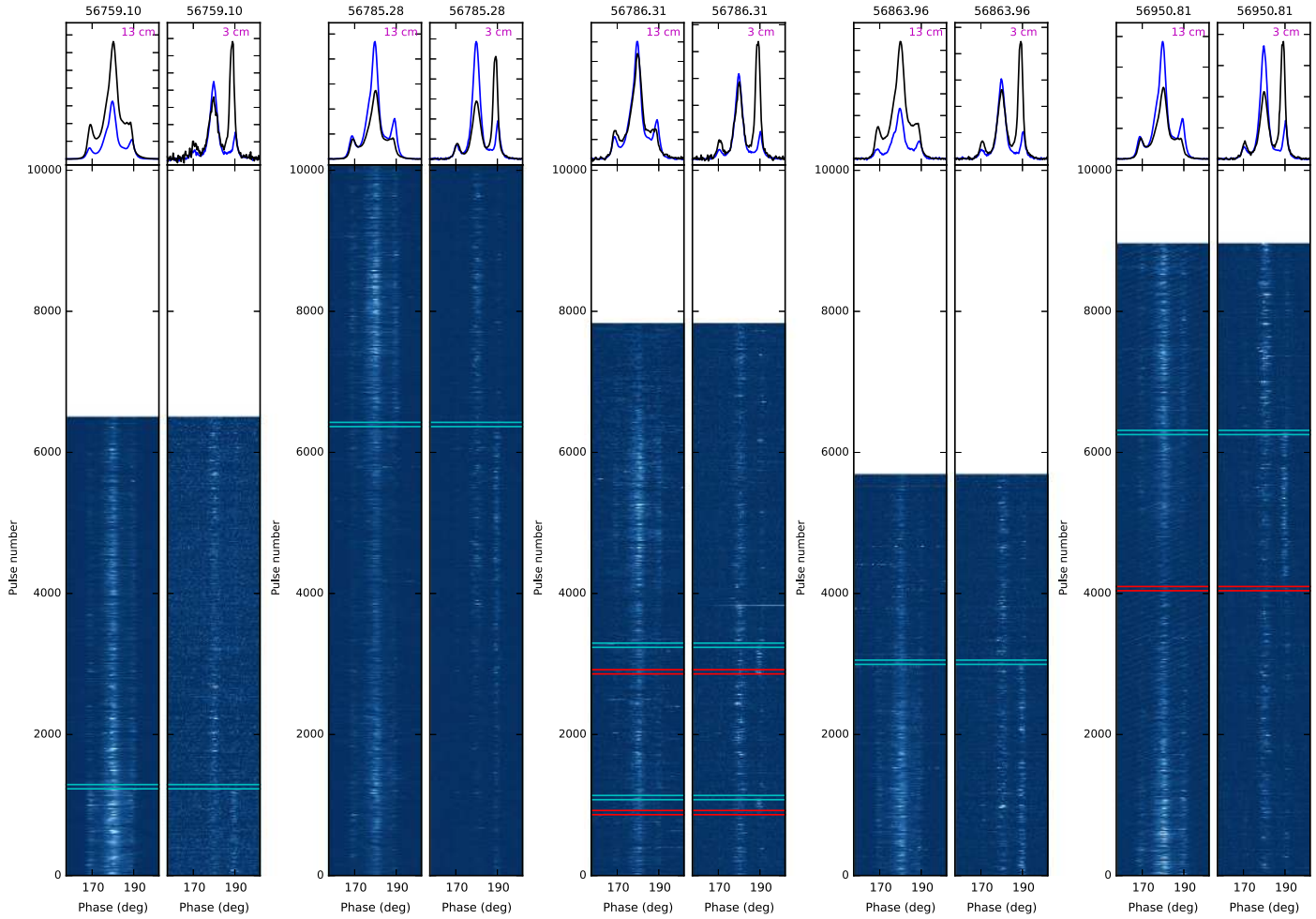

Figure 3. Samples of 13 cm and 3 cm phase-time plots for mode changes of PSR B0329+54. Top panel: the normal (blue) and abnormal (black) mode integrated profiles obtained with all the data of the corresponding mode in that epoch of observation. The MJD and observation band are designated in the top and top right corners, respectively. Bottom panel: phase-time plots of single-pulse data stacked upward. The brightness is linear in flux density, with lighter being stronger. The red line pairs bracket 60 pulses around transitions from normal mode to abnormal mode, and similarly, the cyan line pairs bracket transitions from abnormal mode to normal mode.

changes in the PSR B0329+54 observations. We found that relatively stable integrated profiles of PSR B0329+54 can be obtained by averaging about 300 adjacent pulses. We therefore performed a mode change analysis with the sub-integration time equal to 300 rotational periods. In Figure 2, we show an example of a time sequence of the peak intensity ratios C1/C2 and C3/C2. During this epoch of observation, PSR B0329+54 changed from the abnormal to the normal mode. The plot shows that the ratio C1/C2 exhibited similar variations at both 13 cm and 3 cm, decreasing from 0.28 and 0.26 to 0.19 and 0.12, respectively, during the mode change. Meanwhile, C3/C2 showed very different behavior at 13 cm and 3 cm; it increased from 0.30 to 0.34 at 13 cm but decreased dramatically from 1.60 to 0.33 at 3 cm.

The peak ratio method discussed above cannot identify mode changes shorter than about 300 rotation periods. For strong pulsars like PSR B0329+54, the mode change phenomenon can easily be discerned in the single-pulse phase-time plots in which the pulse strength is expressed with a color gradient. In Figure 3, we present a sample of phase-time plots that show mode changes on MJD 56759.10 ($N = 2$), MJD 56785.28 ($N = 17$), MJD 56786.31 ($N = 20$), MJD 56863.96 ($N = 26$), and MJD 56950.81 ($N = 30$), along with the normal and abnormal mode integrated profiles obtained with all the data of the corresponding mode in that epoch of observation. The time resolution of the phase-time plots is much higher compared with the peak ratio plots shown in Figure 2.

Figure 4 shows expanded views of mode changes for both normal to abnormal (a) and abnormal to normal (b) transitions. Single-pulse profiles across each transition at both 13 cm and 3 cm are shown. These and similar plots for other transitions show that the mode transitions in PSR B0329+54 occurred abruptly and simultaneously at 13 and 3 cm within a few pulse rotational periods.

We applied the two methods discussed above to identify mode changes in the 31 epochs of the TMRT observations (see Table 2). Except for the normal and abnormal pulsar modes described above, there was no evidence for other mode states. Table 2 shows that the abnormal mode was identified in 17 of the 31 observations; two separate bursts were seen in two observations ($N = 16$ and 20). The duration of the abnormal mode ranges between 1.5 minutes and 1.25 hr. Uncertainties in the duration were estimated from the uncertainties in identifying the appearance and disappearance of component C3 in the stacked single-pulse phase-time plots. Summing the abnormal mode times shows that PSR B0329+54 was in the abnormal

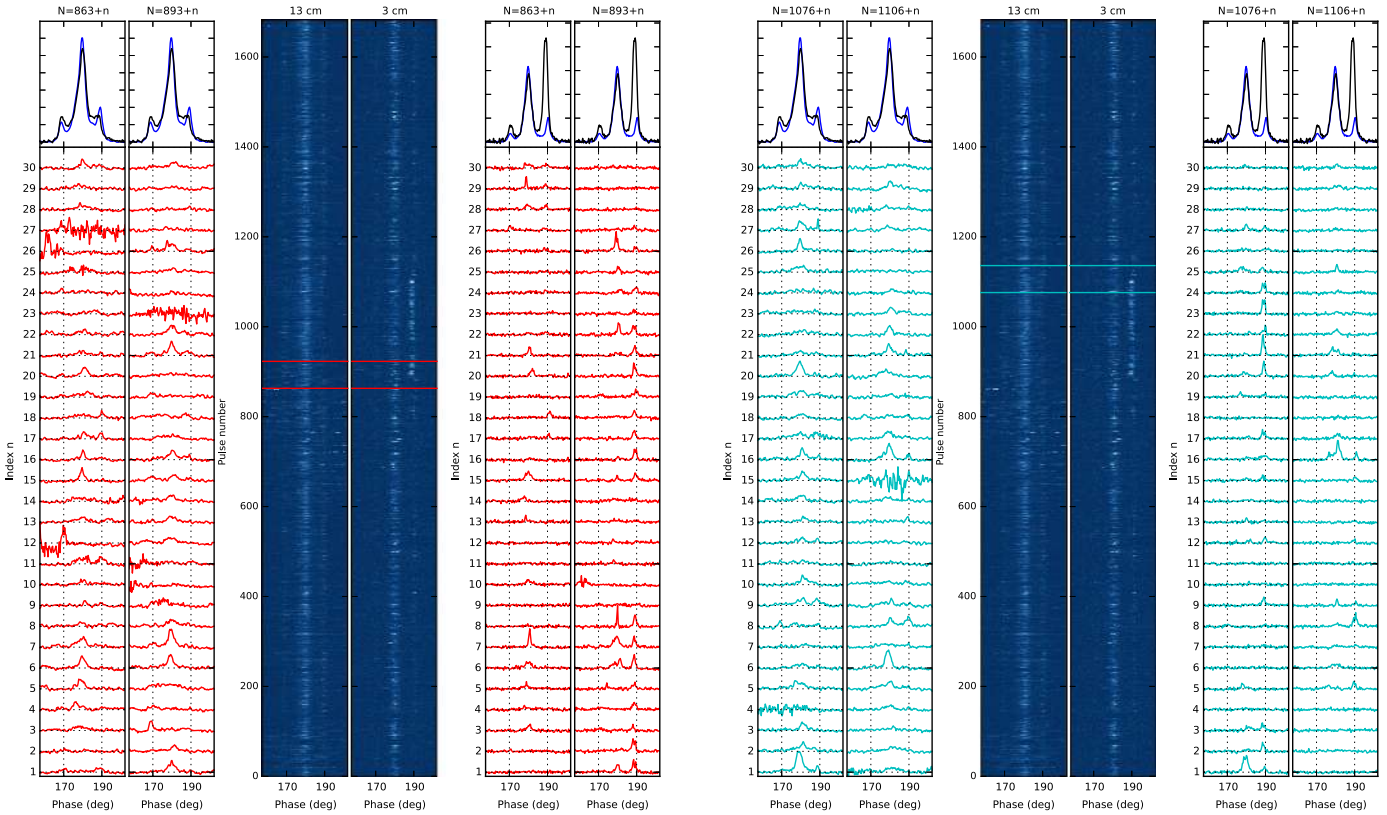

(a) Normal to abnormal mode (b) Abnormal to normal mode

Figure 4. Single-pulse phase-time plots around PSR B0329+54 mode changes. (a) A normal to abnormal mode change at 13 cm (left panels) and 3 cm (right panels). The central color plots show about 1600 pulses around the mode change and the left and right panels show single-pulse profiles for the 60 pulses centered on the change as bracketed by the red lines in the central plots. In both the left (13 cm) and right (3 cm) profile plots, the first 30 pulses are shown in the left sub-panel and the second 30 are shown in the right sub-panel according to the pulse number specifications at the top of each sub-plot. The integrated profiles shown at the top of each sub-panel are for normal (blue) and abnormal (black) modes, obtained with all the data for the corresponding mode and band in that epoch of observation. (b) Similar plots for an abnormal to normal mode transition.

mode for about 13% of the total observing time. This is slightly less than the ∼15% reported previously (Bartel et al. 1982; Chen et al. 2011).

3.2. Quantitative Analysis of Integrated Profiles

The integrated profiles for PSR B0329+54 in the two modes at the two frequency bands shown in Figure 1 are normalized to their peak values. Here, we compare flux density variations in the abnormal and normal modes at the two bands. Flux densities were estimated from the S/N of the data and the theoretical root-mean-square baseline noise using the corresponding SEFD of TMRT given in Section 2. In order to make the flux density changes more easily discernible, the following quantities were estimated:

$$S_{\mathrm{A/N,13\ cm}} = (S_{\mathrm{A,13\ cm}} - S_{\mathrm{N,13\ cm}})/(S_{\mathrm{A,13\ cm}} + S_{\mathrm{N,13\ cm}}), \quad (1)$$

$$S_{\mathrm{A/N,3\ cm}} = (S_{\mathrm{A,3\ cm}} - S_{\mathrm{N,3\ cm}})/(S_{\mathrm{A,3\ cm}} + S_{\mathrm{N,3\ cm}}), \quad (2)$$

where $S_{\mathrm{A,13\ cm}}$, $S_{\mathrm{N,13\ cm}}$, $S_{\mathrm{A,3\ cm}}$, $S_{\mathrm{N,3\ cm}}$ are the mean flux densities at 13 cm and 3 cm in the abnormal and normal modes, respectively. For each calculation, we only used the data from that epoch of observation. This minimizes the effects of uncertain calibration, assuming that the instruments were stable during observations shorter than 2 hr. Derived values of $S_{\mathrm{A/N,13\ cm}}$ and $S_{\mathrm{A/N,3\ cm}}$ are listed in the last two columns of Table 2.

It is clear that $S_{\mathrm{A/N,13\ cm}}$ and $S_{\mathrm{A/N,3\ cm}}$ show different fluctuation properties. The values of $S_{\mathrm{A/N,13\ cm}}$ are quite variable, but seem to distribute randomly around 0.0, whereas almost all the $S_{\mathrm{A/N,3\ cm}}$ values are greater than 0.0, except for that on MJD 56785.12. Quantitatively, the mean value and rms deviation of $S_{\mathrm{A/N,13\ cm}}$ are 0.06 ± 0.32, whereas for $S_{\mathrm{A/N,3\ cm}}$ they are 0.14 ± 0.11. It is clear that the flux density of PSR B0329+54 at 3 cm is larger in the abnormal mode than in the normal mode.

Furthermore, we attempt to quantify parameters of the integrated profiles by fitting five Gaussian components to C1, C2, C3, and the bridge emission, and then calculating the peak flux density ratios $S_{\mathrm{C1/C2}}$ and $S_{\mathrm{C3/C2}}$, and component separations $\Delta\phi_{\mathrm{C1,C2}}$ and $\Delta\phi_{\mathrm{C3,C2}}$. Our results indicate that these quantities are stable from observation to observation, within the uncertainties. Table 3 lists the mean values and their rms deviations across all observations. We also list values of the overall pulse width at 10% of the mean profile peak, W_{10}, derived from the Gaussian components.

4. Narrow Bright Pulses

In the phase-time plots presented in Figure 3, some narrow bright pulses are evident. Similar bright pulses have been detected in several normal pulsars, including PSRs B0656+14 (Weltevrede et al. 2006b), B0943+10 (Backus et al. 2010), and B0031−07 (Karuppusamy et al. 2011), and a small number of

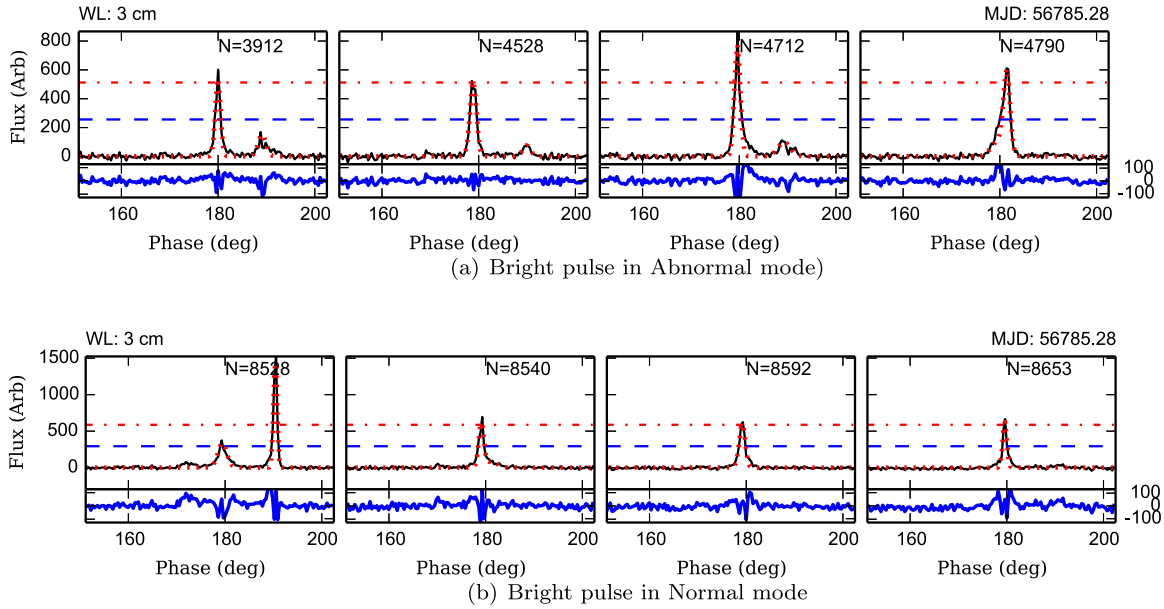

Figure 5. Bright narrow pulses in the 3 cm band from PSR B0329+54. The dashed and dotted–dashed lines are at 5 and 10 times the peak flux density of the integrated profile ($S_{\rm int,pk}$), respectively. The dotted lines show the profiles resulting from the Gaussian fitting. Residuals from these fits are shown in the bottom subpanel of each plot.

Table 3
Parameters for the PSR B0329+54 Integrated Profiles for the Normal and Abnormal Modes and for the 13 cm and 3 cm Bands

Parameter	13 cm		3 cm	
	Normal	Abnormal	Normal	Abnormal
$S_{\rm C1/C2}$	0.19 ± 0.01	0.28 ± 0.01	0.11 ± 0.01	0.26 ± 0.01
$S_{\rm C3/C2}$	0.34 ± 0.01	0.31 ± 0.01	0.33 ± 0.02	1.63 ± 0.05
$\Delta\phi_{\rm C1,C2}$ (°)	10.67 ± 0.06	10.81 ± 0.11	9.52 ± 0.08	9.27 ± 0.13
$\Delta\phi_{\rm C3,C2}$ (°)	9.36 ± 0.09	8.07 ± 0.17	10.51 ± 0.04	9.50 ± 0.10
W_{10} (°)	24.05 ± 0.18	23.30 ± 0.32	22.29 ± 0.21	22.55 ± 0.28
ρ (°)	6.8 ± 0.3	6.6 ± 0.3	6.4 ± 0.3	6.4 ± 0.3
r (km)	213.3 ± 18.3	202.0 ± 19.9	187.4 ± 17.6	191.1 ± 18.8

magnetars, including PSRs J1809−1943 (Serylak et al. 2009), J1622−4950 (Levin et al. 2012), and J1745−2900 (Yan et al. 2015). These pulses are generally 5-10 times the average pulse amplitude, but are not as bright as the "giant" pulses seen in the Crab and other pulsars (e.g., Knight et al. 2006; Mickaliger et al. 2012). True giant pulses are also distinguished by their power-law amplitude distributions as compared to typically lognormal distributions for other pulse emission, including the bright narrow pulses.

Profile plots for a sample of bright pulses from PSR B0329+54 are shown in Figure 5. We fitted Gaussian components to characterize these bright pulses and to determine any quantitative differences from other pulses. The results of this fitting are shown in Figure 5. To quantify the strength of the bright pulses, they are normalized by the peak flux of the corresponding integrated profile ($S_{\rm int,pk}$). As the integrated profile changes with the pulsar mode, pulses obtained in the normal and abnormal modes are treated separately. According to their peak flux density $S_{\rm pk}$, pulses were classified by three groups: <5 times, 5–10 times, and >10 times of $S_{\rm int,pk}$. We found that most of the bright pulses can be fitted with a single Gaussian component. For the sample in Figure 5, we chose pulses whose $S_{\rm pk}$ exceeds 10 times $S_{\rm int,pk}$ in both the normal and abnormal modes.

Compared with the 3 cm results, at 13 cm there were fewer bright pulses with $S_{\rm pk}$ exceeding 10 times of $S_{\rm int,pk}$. For the 3 cm normal and abnormal modes, the occurrence rates were 0.66% and 0.27%, respectively, whereas at 13 cm, the total rate was only about 0.007%.

Both the width at 5 times the rms baseline noise ($W_{5\sigma}$) and the $S_{\rm pk}$ of bright single pulses were obtained from the Gaussian fitting. As Figure 6 shows, stronger single pulses tend to be narrower than average, but there is no clear correlation between the peak flux density and the width of the pulses.

We also performed a statistical analysis on the phase position of bright pulses whose $S_{\rm pk}$ was greater than 10 times $S_{\rm int,pk}$. Data for the two bands and two modes are separately analyzed. In Figure 7, we present the phase distribution of bright pulses occurring in both normal mode and abnormal mode at 3 cm. It is clear that the bright pulses mostly occurred at the phase of the peaks of the corresponding integrated profile. We also detected the same behavior of the narrow bright pulses in the 13 cm data. Finally, we performed a similar statistical analysis on pulses with $S_{\rm pk}$ exceeding 5

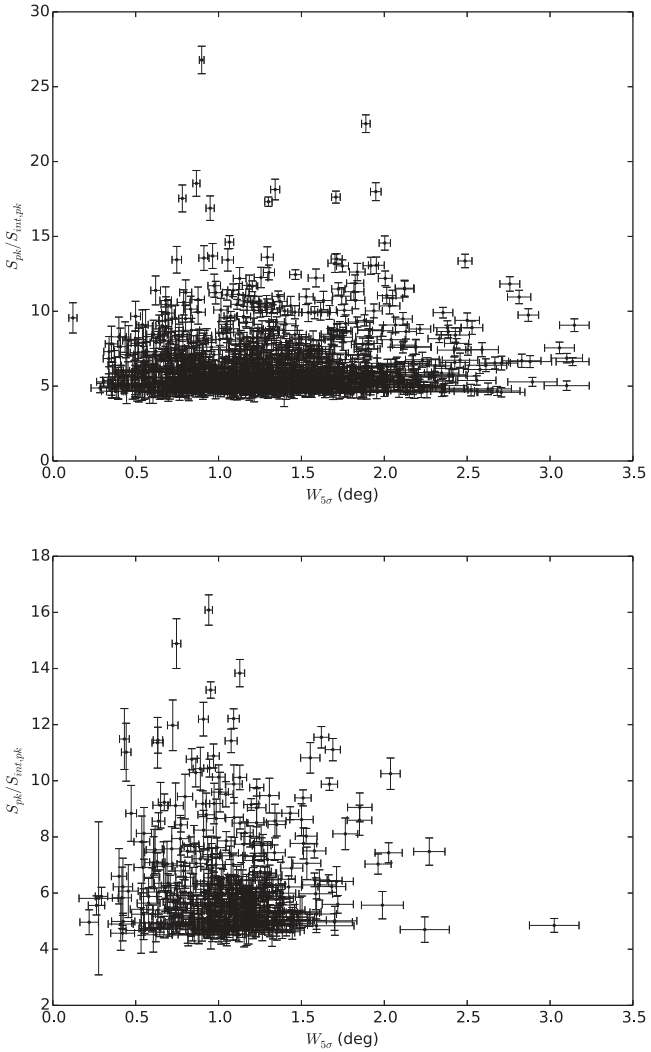

Figure 6. Scatterplots of $W_{5\sigma}$ vs. $S_{\rm pk}/S_{\rm int,pk}$ for single pulses whose peak flux density exceeds $5S_{\rm int,pk}$ for the normal mode (upper panel) and the abnormal mode (lower panel).

times of the $S_{\rm int,pk}$ and found the same behavior in both the normal and abnormal modes.

5. Analysis of Subpulse Drifting in PSR B0329+54

Some pulsars that show mode changes also exhibit drifting subpulses (Wright & Fowler 1981; Redman et al. 2005). Subpulse drifting can be characterized by two parameters along orthogonal directions: the horizontal separation between adjacent subpulses in pulse longitude (P_2) and the vertical separation between drift bands in pulse periods (P_3). It can be detected using an auto-correlation analysis (Taylor et al. 1975) or Fourier analysis (Edwards & Stappers 2002). The longitude-resolved standard deviation (LRSD) and the longitude-resolved modulation index (LRMI) are useful diagnostics of subpulse modulations. Plots from the Fourier analysis, such as the two-dimensional fluctuation spectrum (2DFS) and the longitude-resolved fluctuation spectrum (LRFS), are effective tools to characterize P_2 and P_3 (Weltevrede et al. 2006a, 2007; Weltevrede 2016).

We first applied the auto-correlation analysis method to investigate the subpulse drifting properties of the normal and abnormal modes at both 13 cm and 3 cm, but found no preferred direction for subpulse drifting. We then calculated the LRSD, LRMI, LRFS, and 2DFS values. Besides the 2DFS analysis on the entire phase range of pulsar radiation, the 2DFS of the data corresponding to the phase range of the three peak components (C1, C2, and C3) were calculated individually to investigate the subpulse drifting in these components. We did not attempt to further divide into smaller phase windows in the 2DFS analysis because of the limited sensitivity. In the Fourier analysis, the input pulse series was divided into 256-pulse blocks to improve the sensitivity. Values from the analysis of each block were averaged to give the final results.

In Figure 8, we present the results of the subpulse analyses for the observation at MJD 56785.20 ($N = 16$). In the top panel we show the integrated pulse profiles and the LRMI and LRSD plots. The modulation index has peaks that are greater than 1.0 at the phases of peaks in the integrated profile and is generally higher toward the wings of the profile. The LRFS in the second row shows that in the normal mode at both bands, there is a significant broad red modulation that is concentrated in C2. Such red modulations are commonly observed in core components (Weltevrede et al. 2006a, 2007). When the pulsar is in the abnormal mode (right columns) the situation is quite different. At 13 cm there is still a red modulation, but unlike for the normal mode, it has a broad peak around 0.12 cycles/period (cpp). At 3 cm, there are more significant changes, with a prominent quasi-period modulation at about 0.06 cpp in C3 dominating the integrated spectrum. The red modulation can still be seen in C2, but it appears weaker compared to the normal mode.

The lower two rows of Figure 8 show 2DFS plots for C2 and C3. (The LRFS plots show no significant modulation in C1). The horizontally averaged modulation for C2 at 3 cm shows that the broad quasi-periodic modulation around 0.12 cpp seen in C2 at 13 cm is also present in this component at 3 cm. Although there are some asymmetries in the vertically averaged modulation spectra, they are all centered on zero frequency within the uncertainties. There is therefore no clear evidence for subpulse drifting in this pulsar. However, because of the observed quasi-periodic features, the pulsar can be labeled as type "Dif*" according to the classification of Weltevrede et al. (2006a).

6. Pulse-nulling Analysis

Previous studies indicated that pulse-nulling tends to be more common in the population of pulsars with multi-component integrated profiles, and these pulsars generally have larger characteristic ages (Rankin 1986; Biggs 1992). It was also suggested that pulse-nulling could be a manifestation of mode change, for which one mode has extremely weak radiation (Esamdin et al. 2005; Wang et al. 2007; Sobey et al. 2015). A challenge for nulling analyses is the often limited S/N of single-pulse observations. In our analysis we used the method in Smith (1973) and Ritchings (1976). A pulsar OFF window with the same width as the ON window is selected to quantify the noise properties of the signal. To reduce the effects of interstellar scintillation, a normalized energy is obtained for 500-pulse blocks by dividing by the mean energy of each block. The OFF data in the corresponding block are also divided by the same factor and histograms of the normalized ON and OFF pulsar data are computed. ON and OFF histograms for 13 cm and 3 cm for the observation on MJD 56785.28 ($N = 17$), which has combatively high

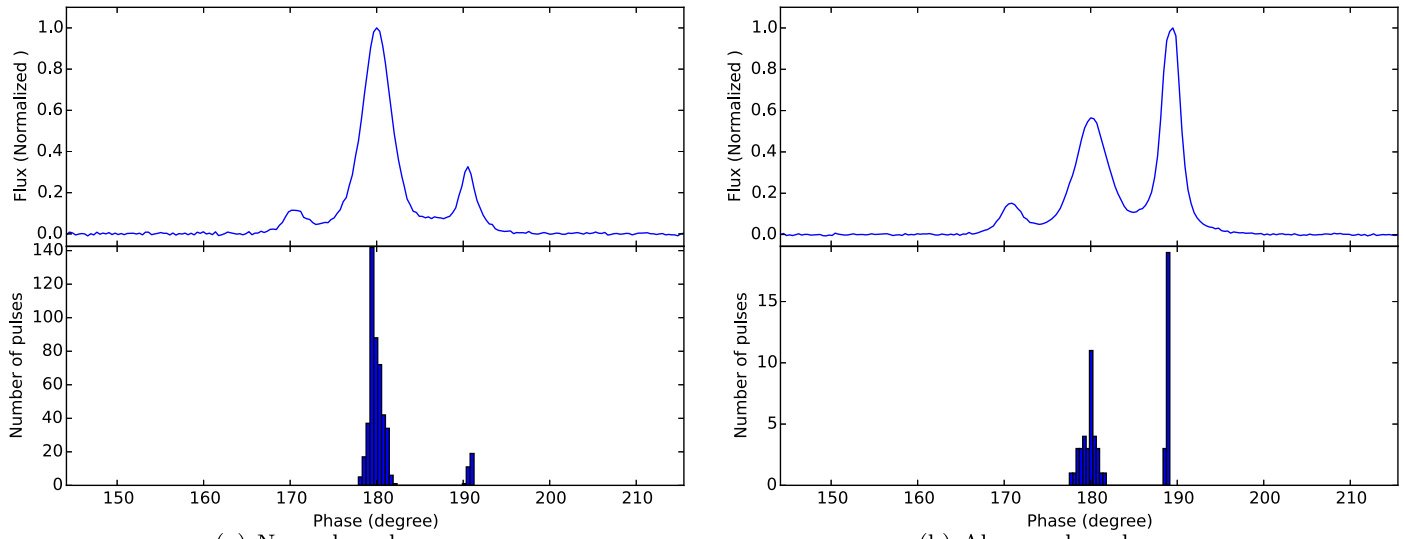

Figure 7. Histogram of the central pulse phase for the PSR B0329+54 3 cm band normal mode and abnormal mode bright pulses with $S_{\rm pk}$ greater than 10 times $S_{\rm int,pk}$. For comparison, the normalized integrated pulse profile for the corresponding mode is shown in the top panel.

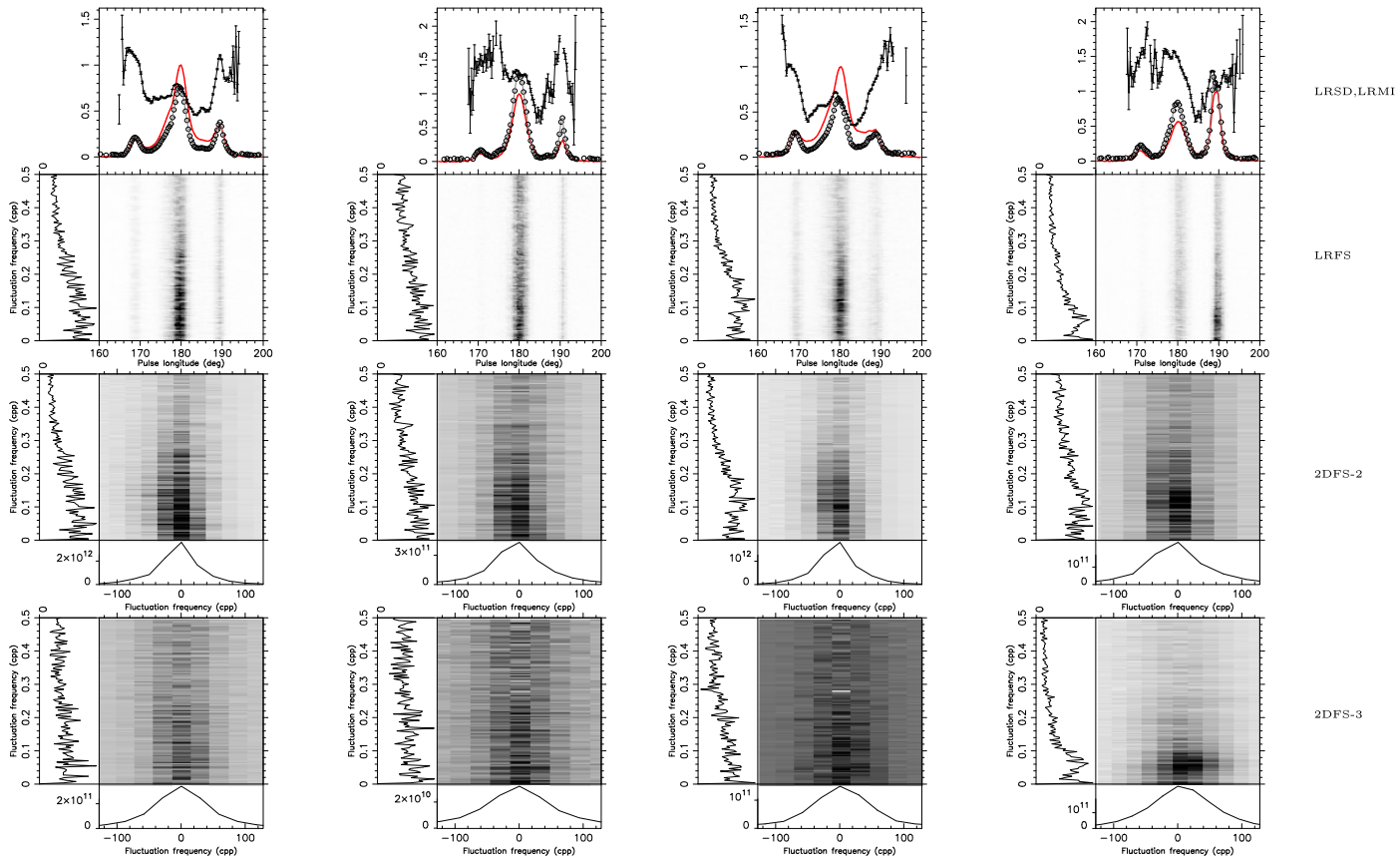

Figure 8. Subpulse drifting analysis results for (a) normal mode and (b) abnormal mode observations at both 13 cm and 3 cm for PSR B0329+54 on MJD 56785.20 ($N = 16$). The top row shows the longitude-resolved rms fluctuation and modulation index, along with the relevant integrated profile (in red). The second row gives the longitude-resolved fluctuation spectrum along with the integrated spectra on the left side of each plot. The third and fourth rows give the two-dimensional fluctuation spectra for C2 and C3, respectively, with the integrated spectra to the left and below.

signal-to-noise ratio, are presented in Figure 9. This figure shows that there was no significant population of null pulses. The procedure for obtaining an upper limit on the null fraction is as follows. An increasing fraction of the OFF probability distribution is subtracted from the ON probability distribution until some portion of the residual distribution becomes either negative or discontinuous. Using this method, we found that the upper limits on the null fraction for PSR B0329+54 are

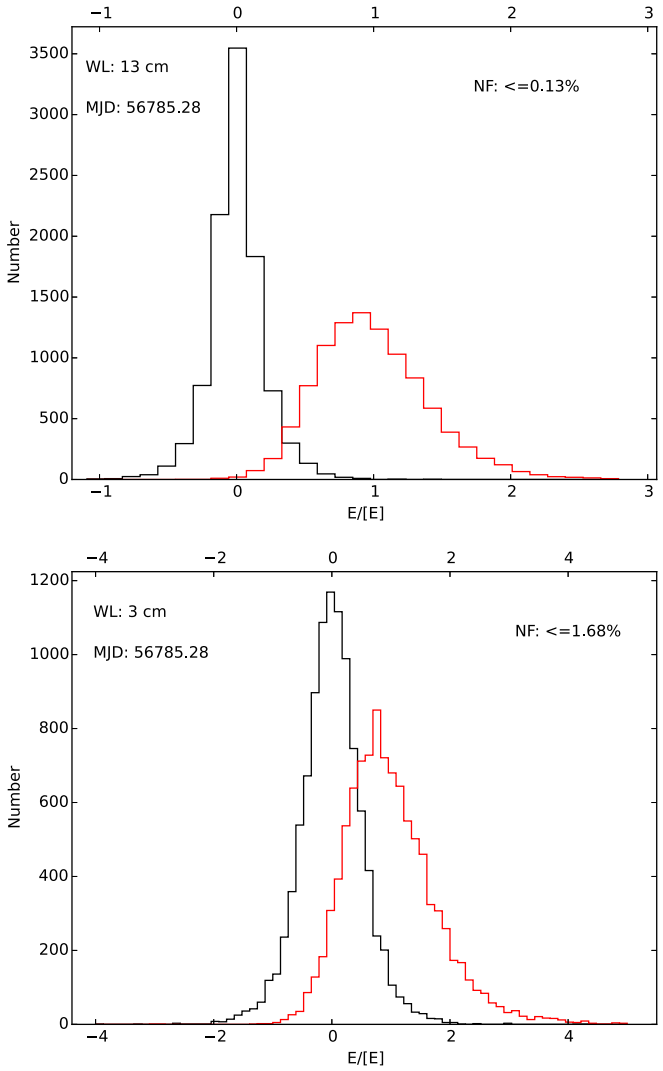

Figure 9. On-pulse (red) and off-pulse (black) pulse-energy histograms for PSR B0329+54 in the 13 cm (upper panel) and 3 cm bands (lower panel) from the observation at MJD 56785.28.

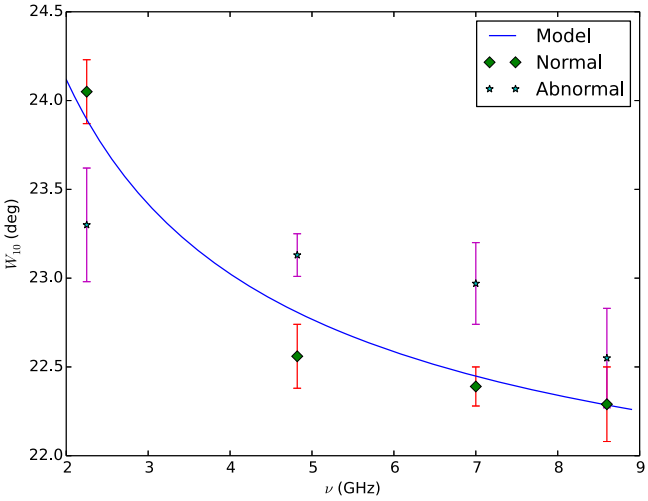

Figure 10. The 10% peak pulse width W_{10} vs. the observation frequency ν. The W_{10} results at 4.8 GHz and 7.0 GHz were also obtained using the TMRT.

0.13% and 1.68% at 13 cm and 3 cm, respectively. This result is consistent with the 0.25% limit obtained at 408 MHz by Ritchings (1976).

7. Discussion and Conclusions

In this study, we obtained 41.6 hr of simultaneous 13 cm and 3 cm single-pulse data for PSR B0329+54 over several epochs with the TMRT. We found two distinct modes of the radio emission, referred to as normal mode and abnormal mode, respectively, with the pulsar in the normal mode 87% of the time. The mode change phenomenon was more obvious at 3 cm than at 13 cm, with the third principal component of the integrated profile, C3, shifted to an earlier phase and substantially stronger in the abnormal mode. On the other hand, at 13 cm, C3 was weaker and became part of a flat "shoulder" connecting to C2 in the abnormal mode. Our results show that the mode switch occurred synchronously at 13 and 3 cm within a few rotation periods. This result is in agreement with previous observations (Bartel et al. 1982).

The shape of the integrated profile of pulsars gives important information about the structure of emission regions in pulsar magnetospheres. In the polar cap model (Goldreich & Julian 1969; Ruderman & Sutherland 1975), the observed radio pulses result from coherent radiation of relativistic particles flowing along dipolar field lines emitted in the tangential direction. The polar cap on the neutron-star surface is defined by the last open magnetic field lines. In this dipolar model, assuming a symmetrically illuminated beam, the opening semi-angle ρ of the pulsar beam corresponding to an overall pulse width W is given by

$$\rho = 2\arcsin[\sin(\alpha+\beta)\sin\alpha\sin^2(W/4) + \sin^2(\beta/2)]^{1/2}, \quad (3)$$

where α is the angle between the rotation and magnetic axes and β is the angle of closest approach of the line of sight to the magnetic axis (Gil et al. 1984). The radio emission altitude, which is the radial distance of the radio emission region measured from the center of the star, can be approximated for small opening angles by

$$r \simeq R_{\rm NS} P(\rho/1.^\circ24)^2, \quad (4)$$

where $R_{\rm NS}$ is the neutron-star radius, P is the pulsar period in seconds, and ρ is the emission cone half-opening angle in degrees (Gil & Kijak 1993).

In Table 3 we give estimates of ρ and r for PSR B0329+54 for the two modes and two bands based on these relations. We take $\alpha = 30.^\circ4 \pm 0.^\circ4$ and $\beta = 2.^\circ5 \pm 0.^\circ4$ (Lyne & Manchester 1988; Rankin 1993) and use values of W_{10} from Table 3. Since the observed pulse widths are somewhat smaller at 3 cm, the derived values of ρ and r are also smaller for emission in this band. There is little or no significant dependence of ρ or r on the emission mode.

The frequency dependence of the pulse width (W_{10}) was studied previously for a large sample of normal pulsars including PSR B0329+54 (Chen & Wang 2014). It was found that the observed W_{10} could be well fit with the relationship

$$W_{10} = A\nu^{\mu} + W_{\rm min}, \quad (5)$$

where the widths are in degrees and the frequency ν is in GHz. For PSR B0329+54, the best-fit coefficient A, index μ, and asymptotic constant $W_{\rm min}$ is $4.^\circ67$, $-0.^\circ68$ and $21.^\circ2$, respectively. Figure 10 shows this model fit along with the observed

W_{10} values at 13 cm (2.3 GHz) and 3 cm (8.6 GHz) from Table 3, along with other TMRT measurements at 4.8 and 7.0 GHz (Z. Yan et al. 2018, in preparation) It can be seen that our results for the normal mode follow the relationship very well, which is expected since the Chen & Wang (2014) results would have been dominated by normal mode emission. However, for the abnormal mode, the frequency dependence is much flatter, with the observed widths narrower at 2.3 GHz, but wider for $\nu > 5$ GHz.

As the last two columns of Table 2 show, the flux densities of the abnormal and normal modes show different fluctuation properties across epochs at 13 cm and 3 cm. The parameter $S_{\mathrm{A/N,13\ cm}}$ was randomly distributed around 0.0, while $S_{\mathrm{A/N,3\ cm}}$ was generally larger than 0.0. We believe that the fluctuation of $S_{\mathrm{A/N,13\ cm}}$ was caused by interstellar scintillation. Based on previous interstellar scintillation results on this pulsar at 1540 MHz (Wang et al. 2008), it can be inferred that the decorrelation bandwidth and typical scintillation timescale at 13 cm are about 50 MHz and 30 minutes, respectively, assuming a Kolmogorov fluctuation spectrum for the interstellar medium. In our case, the 13 cm observations have a bandwidth of 100 MHz and durations of tens of minutes, this only a few "scintiles" were included in the estimate of $S_{\mathrm{A/N,13\ cm}}$. Hence, the effects of interstellar scintillation on the flux density measurements were substantial.

On the other hand, the modulation of $S_{\mathrm{A/N,3\ cm}}$ cannot be simply interpreted as the interstellar scintillation effect. The interstellar scintillation is much weaker at 3 cm (Malofeev et al. 1996). Previous low-frequency diffractive interstellar scintillation observation results on this pulsar (Wang et al. 2008) and related theory (Rickett 1990) suggest a timescale of 1.6 hr for the weak interstellar scintillation. Although the scintillation effects were still evident, if scintillation were the main cause of the variations, the average ratio would be around 0.0. In fact, $S_{\mathrm{A/N,3\ cm}}$ were almost always greater than 0.0. This reflects an intrinsic flux density variation between the normal and abnormal pulsar modes, largely due to the flux enhancement of C3 in the abnormal mode at 3 cm.

Previous studies found possible correlations between mode changes and subpulse drifting. Our multi-epoch observations indicated that, in the abnormal mode, PSR B0329+54 showed evidence for quasi-periodic fluctuations. For C2 there was a broad spectral feature centered around 0.12 cpp, corresponding to a P_3 in the range of 5–20 periods. For C3, no quasi-period modulation was evident, but at 3 cm there was a clear feature centered at 0.06 cpp, that is, $P_3 \sim 15$ pulse periods. This feature was not seen in previous studies at 21 and 92 cm (Weltevrede et al. 2006a, 2007). Although the 2D fluctuation spectra had some asymmetry when integrated vertically, in general there was no significant offset from zero, and hence no evidence for pulse drifting. Previous low-frequency observations are also consistent with no preferred drifting directions for this pulsar.

We found no evidence for pulse-nulling in PSR B0329+54, with upper limits on the null fraction of 0.13% and 1.68% at 13 cm and 3 cm, respectively. The higher limit at 3 cm is principally because of the lower S/N of these observations. Previous low-frequency (408 MHz) observations gave a consistent limit on the null fraction of 0.25% (Ritchings 1976). It is clear that PSR B0329+54 is a pulsar with very a low probability of nulling. Previous investigations indicated that pulsar null fractions correlate more with the characteristic age than with the pulse period (Wang et al. 2007). Given that the characteristic age of PSR B0329+54 is 5.53 Myr (Hobbs et al. 2004), a low null fraction is not surprising.

Single-pulse analyses show the existence of occasional narrow bright pulses that seem to be a statistically separate population compared from the distribution of other single pulses. Figure 6 shows that strong single pulses tend to be narrower than the average width, although there is no clear correlation between width and strength. Though the peak amplitudes of these bright pulses are relatively high, their total power is not as strong as the giant pulses detected in a few pulsars such as the Crab pulsar (Knight 2006 and references therein). In PSR B0329+54, the bright pulses preferentially occur at the pulse phases of the second and third peaks of the integrated profile. The burst rate at 3 cm is up to 100 times higher than that at 13 cm. This suggests a real difference in the coherence properties of the emission process for observed frequencies around 10 GHz compared to lower frequencies, possibly related to an emission location closer to the neutron-star surface. Future studies with simultaneous multi-frequency observations of a large pulsar sample will be important for helping to understand these differences.

This work was supported in part by the National Natural Science Foundation of China (grants U1631122, 11403073, and 11633007), the National Basic Research Program of China (973 program) No. 2012CB821806, the Strategic Priority Research Program "The Emergence of Cosmological Structures" of the Chinese Academy of Sciences, grant No. XDB09000000, the Knowledge Innovation Program of the Chinese Academy of Sciences (grant No. KJCX1-YW-18), and the Scientific Program of Shanghai Municipality (08DZ1160100). We thank the anonymous referee for the helpful suggestions.

ORCID iDs

Zhen Yan (闫振) https://orcid.org/0000-0002-9322-9319
R. N. Manchester https://orcid.org/0000-0001-9445-5732
C.-Y. Ng https://orcid.org/0000-0002-5847-2612

References

Anish Roshi, D., Bloss, M., Brandt, P., et al. 2012, arXiv:1202.0938
Backer, D. C. 1970, Natur, 228, 1297
Backus, I., Mitra, D., & Rankin, J. M. 2010, MNRAS, 404, 30
Bartel, N., Morris, D., Sieber, W., & Hankins, T. H. 1982, ApJ, 258, 776
Bartel, N., & Sieber, W. 1978, A&A, 70, 307
Biggs, J. D. 1992, ApJ, 394, 574
Burke-Spolaor, S., Johnston, S., Bailes, M., et al. 2012, MNRAS, 423, 1351
Chen, J. L., & Wang, H. G. 2014, ApJS, 215, 11
Chen, J. L., Wang, H. G., Wang, N., et al. 2011, ApJ, 741, 48
DuPlain, R., Ransom, S., Demorest, P., et al. 2008, Proc. SPIE, 7019, 70191D
Edwards, R. T., & Stappers, B. W. 2002, A&A, 393, 733
Esamdin, A., Lyne, A. G., Graham-Smith, F., et al. 2005, MNRAS, 356, 59
Ferguson, D. C., Boriakoff, V., Weisberg, J. M., Backus, P. R., & Cordes, J. M. 1981, A&A, 94, 16
Gil, J., & Kijak, K. 1993, A&A, 273, 563
Gil, J. A., Gronkowski, P., & Rudnicki, W. 1984, A&A, 132, 312
Goldreich, P., & Julian, W. H. 1969, ApJ, 157, 869
Hassall, T. E., Stappers, B. W., Hessels, J. W. T., et al. 2012, A&A, 543, A66
Helfand, D. J., Manchester, R. N., & Taylor, J. H. 1975, ApJ, 198, 661
Hobbs, G., Lyne, A. G., Kramer, M., Martin, C. E., & Jordan, C. 2004, MNRAS, 353, 1311
Hobbs, G. B., Edwards, R. T., & Manchester, R. N. 2006, MNRAS, 369, 655
Hotan, A. W., van Straten, W., & Manchester, R. N. 2004, PASA, 21, 302
Janssen, G. H., & van Leeuwen, J. 2004, A&A, 425, 255
Karuppusamy, R., Stappers, B. W., & Serylak, M. 2011, A&A, 525, A55

Knight, H. S. 2006, ChJAS, 6, 41
Knight, H. S., Bailes, M., Manchester, R. N., Ord, S. M., & Jacoby, B. A. 2006, ApJ, 640, 941
Kramer, M. 1994, A&AS, 107, 527
Kramer, M., Jessner, A., Doroshenko, O., & Wielebinski, R. 1997, ApJ, 489, 364
Kramer, M., Xilouris, K. M., Jessner, A., Wielebinski, R., & Timofeev, M. 1996, A&A, 306, 867
Levin, L., Bailes, M., Bates, S. D., et al. 2012, MNRAS, 422, 2489
Lorimer, D. R., Yates, J. A., Lyne, A. G., & Gould, D. M. 1995, MNRAS, 273, 411
Lyne, A. G. 1971, in IAU Symp. 46, The Crab Nebula, ed. R. D. Davies & F. G. Smith (Dordrecht: Reidel), 182
Lyne, A. G., & Manchester, R. N. 1988, MNRAS, 234, 477
Malofeev, V. M., Shishov, V. I., Sieber, W., et al. 1996, A&A, 308, 180
Manchester, R. N., Hobbs, G. B., Teoh, A., & Hobbs, M. 2005, AJ, 129, 1993
Mickaliger, M. B., McLaughlin, M. A., Lorimer, D. R., et al. 2012, ApJ, 760, 64
Morris, D., Graham, D. A., & Bartel, N. 1981, MNRAS, 194, 7P
Rankin, J. M. 1986, ApJ, 301, 901
Rankin, J. M. 1993, ApJS, 85, 145
Redman, S. L., Wright, G. A. E., & Rankin, J. M. 2005, MNRAS, 357, 859
Rickett, B. J. 1990, ARA&A, 28, 561
Ritchings, R. T. 1976, MNRAS, 176, 249
Ruderman, M. A., & Sutherland, P. G. 1975, ApJ, 196, 51
Serylak, M., Stappers, B. W., Weltevrede, P., et al. 2009, MNRAS, 394, 295
Smith, F. G. 1973, MNRAS, 161, 9P
Smits, J. M., Mitra, D., & Kuijpers, J. 2005, A&A, 440, 683
Sobey, C., Young, N. J., Hessels, J. W. T., et al. 2015, MNRAS, 451, 2493
Taylor, J. H., Manchester, R. N., & Huguenin, G. R. 1975, ApJ, 195, 513
van Leeuwen, A. G. J., Kouwenhoven, M. L. A., Ramachandran, R., Rankin, J. M., & Stappers, B. W. 2002, A&A, 387, 169
Wang, N., Manchester, R. N., & Johnston, S. 2007, MNRAS, 377, 1383
Wang, N., Yan, Z., Manchester, R. N., & Wang, H. X. 2008, MNRAS, 385, 1393
Weltevrede, P. 2016, A&A, 590, A109
Weltevrede, P., Edwards, R. T., & Stappers, B. W. 2006a, A&A, 445, 243
Weltevrede, P., Stappers, B. W., & Edwards, R. T. 2007, A&A, 469, 607
Weltevrede, P., Stappers, B. W., Rankin, J. M., & Wright, G. A. E. 2006b, ApJL, 645, L149
Wright, G. A., & Fowler, L. A. 1981, A&A, 101, 356
Xilouris, K. M., Seiradakis, J. H., Gil, J. A., Sieber, W., & Wielebinski, R. 1995, A&A, 293, 153
Yan, Z., Shen, Z.-Q., Wu, X.-J., et al. 2015, ApJ, 814, 5
Yao, J. M., Manchester, R. N., & Wang, N. 2017, ApJ, 835, 29